Journal of Materials Chemistry A

Accepted Manuscript

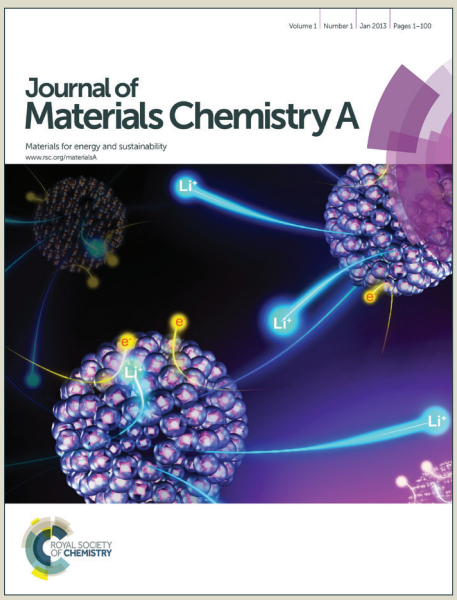

ROYAL SOCIETY OF CHEMISTRY

www.rsc.org/materialsA

Journal of Materials Chemistry A

Journal of Materials Chemistry A

Dynamic Article Links ►

Cite this: DOI: 10.1039/c0xx00000x

ARTICLE TYPE

www.rsc.org/xxxxxx

Crystal Plane Effect of CoFe Nanocrystals on Fischer-Tropsch Synthesis

Jiaqiang Sun,*[a] Shenke Zheng,[a,b] Kui Zhang,[a] Dechen Song,[b] Yanting Liu,[a] Xiaodong Sun[a] and Jiangang Chen[a]

Received (in XXX, XXX) Xth XXXXXXXXX 20XX, Accepted Xth XXXXXXXXX 20XX

DOI: 10.1039/b000000x

Both CoFe nanowires and nanosheets with preferentially exposed distinguished crystal planes have been fabricated to investigate the crystal plane sensitivity in catalysis. CoFe nanowires and nanosheets are obtained by a stepwise topotactic transformation involving the hydrothermal treatment and thermal decomposition of iron-doped cobalt carbonate hydroxide hydrate intermediate on an iron substrate, and subsequent reduction of cobalt iron oxides. The CoFe nanowires and nanosheets show different catalytic activities for Fischer-Tropsch synthesis. The CO conversion is 44% over nanowires and 13% over nanosheets at 300 °C, with the corresponding mass specific rates of CO consumption being 10.18 and 2.98 $\mu mol \cdot g^{-1} \cdot s^{-1}$, respectively. The excellent performance of nanowires is ascribed to the large fraction of active (110) crystal planes. The TOF of Co atom on {110} crystal planes is 8.2×10^{-2} s^{-1} at 300 °C, which is 2.6 times higher than that on $\{\bar{1}11\}$ crystal planes.

1. Introduction

Fischer–Tropsch (FT) synthesis has received considerable attention from both academic researchers and industrial engineers, primarily because of the increasingly stringent environmental requirements.[1] The fundamental processes occurring on the surface of catalysts need to be better understood since FT synthesis is a complex gas-liquid-solid multiphase reaction. The past decade has seen the major advances in the understanding of the structure sensitivity of a wide variety of reactions.[2-8] The reactivity and selectivity of catalysts depend greatly upon the arrangement of surface atoms on different crystal planes. Research on FT synthesis on Co single crystals has been carried out mainly by researchers at Shell. For instance, Geerlings et al. conducted work on bulk Co single crystals with different exposed crystal planes.[9-12] The authors first studied FT synthesis on Co (0001) in the temperature range between 220 °C and 300 °C at 0.1 MPa total pressure and an H_2 : CO ratio of 2 : 1.[9-11] Under these reaction conditions methane is the major product, with little heavier hydrocarbons. Following experiments showed that the activation energies for methane, ethane and propane formation were equal, suggesting similar rate determining steps. The structure sensitivity of FT synthesis was investigated by comparing the catalytic behavior on grooved $(11\bar{2}0)$ and stepped $(10\bar{1}2)$ cobalt surface with that on the close-packed Co (0001) surface.[9, 12] The activation energies for methane and ethane formation on Co $(11\bar{2}0)$ are both 70 kJ/mol, which is identical to the values observed on Co (0001). While Co $(11\bar{2}0)$ yields a slightly larger chain growth probability than Co (0001) (0.36 compared to 0.30 at 250 °C), because of rapid olefin hydrogenation on the close-packed surface, which prevents olefin readsorption reactions and leads to the lower chain growth probability on Co (0001).[13] Besides, based on a first-principle kinetic study, Hexagonal close-packed (hcp) Co catalysts have remarkably higher intrinsic activity than face-centered cubic (fcc) Co catalysts, and hcp Co catalysts prefer the direct dissociation route while fcc Co catalysts prefer the H-assisted route for CO activation in the presence of hydrogen.[14] In surface science, well-defined single-crystal surfaces are studied by applying physical techniques under ultralow-pressure conditions. However, these model systems differ significantly from real catalytic conditions, both with regard to the nature of the catalyst surface ("materials gap") and the applied pressure range ("pressure gap").[15-17] Hence, the synthesis of shape-controlled nanocrystals with well-defined surfaces adopting simple and conventional experimental methods rather than high vacuum physical technique, could be employed for pursuing mechanisms under real operating conditions.

Furthermore, in FT synthesis both external transfer and intraparticle diffusion influence the intrinsic reactivity greatly. So the catalyst research should also consider the macroscopic diffusion effect and heat transfer. The metallic monolith substrate coating with conventional catalytic layer has been applied into FT synthesis in order to overcome the diffusion and heat transfer limitations.[18, 19] However, it remains as a problem with regards to inhomogeneous distribution of the active component on the monolith and weak adhesion between the metal substrate and washcoat.[20-22, 23] Thus, designing and synthesizing novel structured catalysts with high reactivity and stability remain a challenging goal in heterogeneous catalysis. The development of nanotechnology in recent decades brings new opportunities in the exploration of high-performance catalysts.[24] Uniform structured nanocrystals with the catalytically active component directly

grown on a metal substrate have a homogeneous distribution of the active material and good binding of the active material with the substrate, ideally allowing its catalytic properties to be maintained even under high temperature reaction conditions. Therefore, the uniform nanocrystals with more reactive crystal planes exposed, directly grown on a metal substrate, should be an effective architecture for a structured catalyst.

Herein, we report the synthesis of CoFe nanocrystals grown on substrate and their catalytic activity in the FT synthesis. The structure of the catalyst offers several advantages: First, CoFe nanocrystals obtained by transformation of iron-doped cobalt carbonate hydroxide hydrate precursors have predominantly exposed {110} planes, maximizing the favorable active sites at the surface. Second, the CoFe is grown directly on a metal (iron) substrate, which avoids the irregular distribution of the active component which tends to occur in any coating process. The direct contact of the nanocrystals to the underlying substrate also ensures the catalyst is strongly anchored thus mitigating leaching during the catalytic reactions. The synthesis of these nanocrystals with their highly active crystal planes highlights new opportunities for the design of novel types of highly efficient structured catalysts.

2. Experimental

2.1 Catalyst Preparation

All chemicals were of analytical grade and were used as received without further purification.

In a typical synthesis, 10 mmol of $Co(NO_3)_2 \cdot 6H_2O$, 20 mmol of NH_4F, and 50 mmol of hexamethylenetetramine (HMT) were dissolved in 100 mL of water under stirring. The homogeneous solution prepared above was transferred into a Teflon-lined stainless steel autoclave. The iron substrate was carefully cleaned with HCl (1 $mol \cdot L^{-1}$), absolute ethanol, and distilled water. After the cleaned iron substrate was immersed in the homogeneous solution, the autoclave was sealed and maintained at 160 °C for 4 h and then allowed to cool down to room temperature naturally. The substrate was washed several times with distilled water, dried at 80 °C for 2 h, and calcined in air at 300 °C for 4 h. Finally the CoFe nanowires(15 g) were reduced at 400 °C and 2 MPa for 4 h by H_2 with a gas hourly space velocity (GHSV) of 12 $L \cdot h^{-1} \cdot g^{-1}$ in a stainless fixed-bed reactor with an inner diameter of 10 mm. CoFe nanosheets were obtained by increasing hydrothermal reaction time to 8 h and subsequent using a similar process described above.

2.2 Characterization

Powder X-ray diffraction (XRD) was performed on a Shimadzu XRD-6000 diffractometer with Cu Kα radiation (λ = 1.5418 Å) in the 2θ range from 5° to 85°. The size and morphology of as-synthesized samples were monitored by using a scanning electron microscope (SEM, Zeiss Supra 55). The structure and composition of the products were characterized by means of a high-resolution transmission electron microscope (HRTEM, JEM 2100F) and energy dispersive X-ray spectroscopy (EDS). Samples were prepared by scraping the cobalt iron from the substrate and ultrasonicating in ethanol, after which the suspension was dropped onto a carbon-enhanced copper grid and dried in air. The content of Co and Fe was also analyzed by inductively coupled plasma atomic emission spectroscopy (ICP-AES, Thermo iCAP6300). The surface area was determined by BET (Brunauer–Emmett–Teller) measurements using a Tristar Ⅱ 3020 N_2 adsorption analyzer. The precursor (30 mg) was placed in a quartz reactor and was reduced by a 5% H_2/N_2 gas mixture at a flow rate of 50 $mL \cdot min^{-1}$, as the TPR experiments were performed. The temperature was ramped at 10 $°C \cdot min^{-1}$ to the final temperature and the hydrogen consumption was recorded using a thermal conductivity detector (TCD).

2.3 Catalytic Reaction

The catalytic behavior in FT synthesis was also studied in a fixed bed reactor. The electrically heated vertical stainless steel tubular reactor is cladded with a 50 cm copper cylinder, to assure that the reactor wall around the fixed bed is isothermal. The reactor can be supplied with hydrogen, CO_2, synthesis gas (molar ratio $H_2/CO=2$). The gas flow is controlled by Books 5850E mass flow controllers (MFC). The pressure is controlled via a back pressure regulator. The reaction products pass a 130 °C hot trap and a 5 °C cooling trap at working pressure and can be measured online by a GC. After in-situ reduction, the catalysts were cooled to 50 °C, the synthesis gas (molar ratio H_2/CO = 2, GHSV = 6 $L \cdot h^{-1} \cdot g^{-1}$) was fed into the catalyst bed and the temperature was increased at 1.0 $°C \cdot min^{-1}$ heating rate to 300 °C. During testing, the pressure of synthesis gas was maintained at 2.0 MPa. The FT reaction rates and hydrocarbon selectivity were evaluated after 24 h on-stream. The gaseous reaction products were analyzed on-line by gas chromatography (GC 920). Analysis of H_2, CO, CO_2, CH_4 and N_2 was performed using a carbon molecular sieve column and a thermal conductivity detector. Hydrocarbons (C_1-C_8) were separated in a capillary porapack-Q column and analyzed by a flame ionization detector.

3. Results and discussion

The CoFe nanowires and nanosheets on iron substrate were achieved by a stepwise topotactic transformation process based on fabrication of hierarchical $Co_{3-x}Fe_xO_4$ nanowire arrays on an iron substrate,[5, 25] as illustrated in Figure 1a. An iron substrate was immersed in a solution containing a mixture of Co^{2+} and F^- ions and HMT. Hydrolysis of the HMT under hydrothermal conditions resulted in the growth of iron-doped orthorhombic cobalt carbonate hydroxide hydrate nanowires grown on the substrate. Continued reaction resulted in the formation of nanosheets of iron-doped orthorhombic cobalt carbonate hydroxide hydrate. Finally the cobalt iron nanowires and nanosheets were obtained by calcination of the precursors in air and reduction in H_2. The images shown in Figure 1b illustrate that the iron-doped orthorhombic cobalt carbonate hydroxide hydrate on the film can not be dislodged after 2 h of ultrasonication, implying the strong interaction between the precursors and the metallic substrate. The scanning electron microscopy (SEM) images in Figure 1c-f clearly show the morphology evolution of the CoFe nanocrystals on the iron substrate. After the hydrothermal reaction of the iron substrate in the reaction mixture at 160 °C for 4 h, well-defined cuboid nanowires knitted net on the iron substrate was obtained (Figures 1c and 1d). The cuboid nanowires are about 10 μm in length, approximately 60 nm in thickness and 60 nm in width. After hydrothermal reaction for

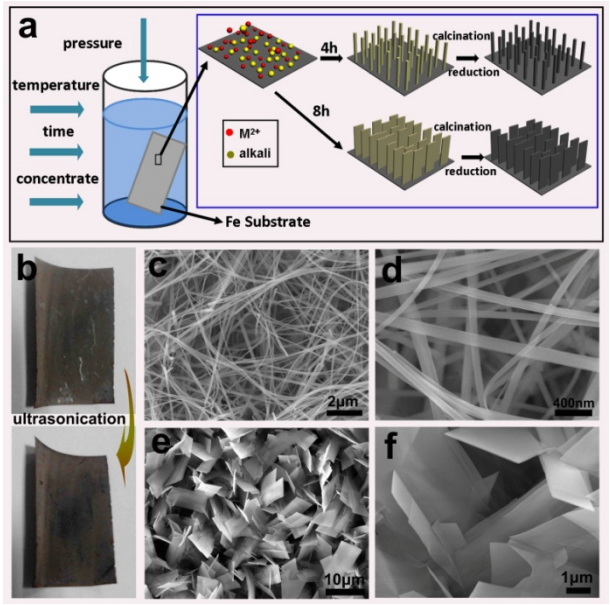

Figure 1 (a) Schematic mechanism of the growth process of CoFe nanocrystals on the iron substrate; (b) images of a sample before and after 2 h ultrasonication; SEM images of the samples formed on the iron substrate after different reaction time: (c, d) 4 h; (e, f) 8 h.

another 4 h, the nanowires gradually grew into shorter and wider nanosheets with an average thickness, width and length of approximately 30 nm, 3 μm and 6 μm, respectively, as displayed in Figures 1e and 1f. We consider that the synthesis of iron-doped orthorhombic cobalt carbonate hydroxide hydrate is a prerequisite for the achievement of single-crystalline body-centered cubic (bcc) CoFe nanowires and nanosheets on iron substrate. NH_4F is considered to play an important role in the formation of the iron-doped cobalt carbonate hydroxide hydrate. Initially, Fe^{3+} ions adsorbed on the surface of the iron substrate were fully coordinated with F^- to form $[FeF_6]^{3-}$. With the increasing of the reactant temperature, HMT hydrolyzed into formaldehyde and ammonia, acting as a pH buffer to slowly release OH^-. It resulted in a slow release of Fe^{3+} ions from $[FeF_6]^{3-}$, bonding on the Fe substrate. The as-formed iron-doped cobalt carbonate hydroxide hydrate crystal seeds sticked firmly to the iron substrate with the assistance of $[FeF_6]^{3-}$. Addition of NH_4F serves both to activate the iron substrate and lead to a strong adhesion between the final nanocrystal and the substrate.

Along with SEM observations, the phases of the as-prepared samples were examined by the XRD (Figure 2). All the diffraction peaks of the precursor indicated that these two samples are the iron-doped orthorhombic cobalt carbonate hydroxide hydrate. All the peaks in the diffraction pattern have slightly larger 2θ values compared with the standard XRD pattern of cobalt carbonate hydroxide hydrate (JCPDS card, no. 48-0083, the peaks marked "*" stand for the Fe substrate), which can be attributed to the substitution by iron of some of the cobalt ions in cobalt carbonate hydroxide hydrate. After calcination, the original brown film became completely black. All the peaks in the XRD pattern shown in Figure 2c and 2d can be indexed as the face-centered cubic (fcc) phase (JCPDS card, no. 74-3417) of a spinel $Co_{3-x}Fe_xO_4$, with a lattice constant a = 8.065 Å, with no other byproducts being detected. High-resolution TEM (HRTEM) and SAED were used to further confirm the phase of the

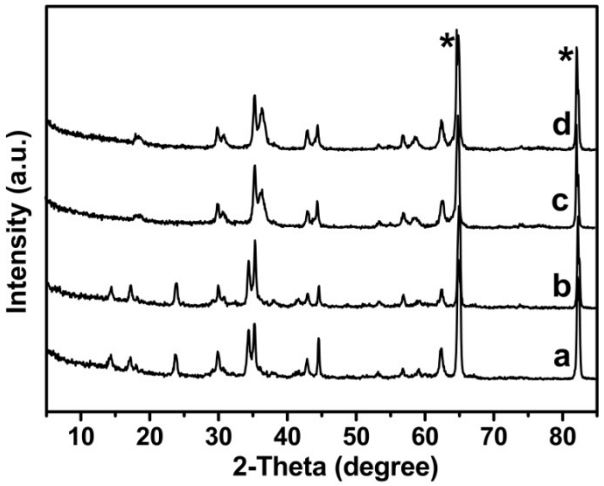

Figure 2 XRD patterns of the nanowires before (a) and after calcinations (c); XRD patterns of the nanosheets before (b) and after calcinations (d).

nanowires and nanosheets precursor. As shown in Figures 3b, an interplanar spacing of 0.88 nm was detected for an individual nanowire formed after 4 h, corresponding to the (100) plane of iron-doped orthorhombic cobalt carbonate hydroxide hydrate. The interplanar spacing of 0.44 nm was detected for an individual nanosheet formed after 8 h, corresponding to the (001) plane of iron-doped orthorhombic cobalt carbonate hydroxide hydrate (Figure 3e). Combining the HRTEM and corresponding SAED analysis (Figure 3c, 3f), single-crystalline iron-doped cobalt carbonate hydroxide hydrate nanowires and nanosheets grown along the [010] and [001] direction can be identified respectively. The Fe-doping level was measured by ICP analysis, which shows the atomic ratio of Co/Fe of nanowires and nanosheets to be around 1.47 and 1.40 respectively.

After reduction, all the peaks in the XRD pattern shown in Figure 4a can be indexed as the body-centered cubic (bcc) phase (JCPDS card, no. 48-1818) of a cobalt iron, with a lattice constant a = 2.842 Å, with no other phase being detected. As shown in Figure 4b, 4c and 4f, the CoFe nanowires and nanosheets are obtained without altering the original morphology of the iron-doped cobalt carbonate hydroxide hydrate precursor. However, they experienced a transformation in chemical composition and crystal structure from iron-doped orthorhombic cobalt carbonate

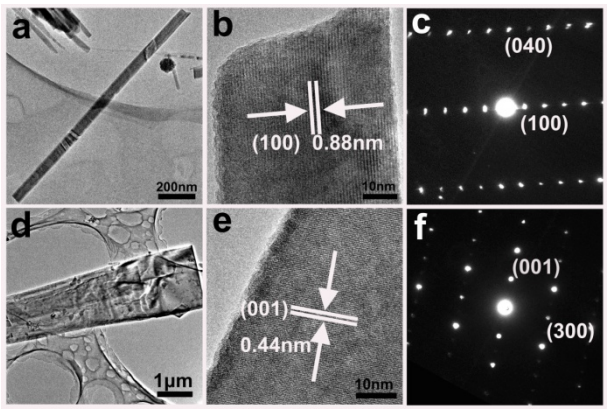

Figure 3 HRTEM (a, b) and SAED (c) images of the iron-doped cobalt carbonate hydroxide hydrate nanowires; HRTEM (d, e) and SAED (f) images of the iron-doped cobalt carbonate hydroxide hydrate nanosheets.

hydroxide hydrate to bcc CoFe. The temperature is an essential factor in determining the shape of the CoFe nanocrystals by altering the reduction rate of $Co_{3-x}Fe_xO_4$ and the growth rate of CoFe nanocrystals during the reduction process. As shown in Figure S1, because of the Rayleigh instability, the nanosheets transform into CoFe polycrystal, when the temperature is increased at 10.0 °C·min^{-1} heating rate to 400 °C.[26] When the temperature is increased at 1.0 °C·min^{-1}, the morphology of the nanosheets can be remained. The nanowires also have a similar behaviour. Apparently, both the reduction rate of $Co_{3-x}Fe_xO_4$ and the growth rate of CoFe nanocrystals increased with temperature; the relative ratio of the rates for these two elementary steps determined the shape of the CoFe nanomaterials.[27, 28] In the enlarged image, shown in Figures 4b, it can be clearly seen that the nanowires have a regular rectangular cross-section with a thickness of 60 nm and width of 60 nm. The interplanar spacing of 0.20 nm is detected for the nanowire and nanosheet, corresponding to the (110) plane of cubic CoFe, as indicated in Figure 4d and 4g. The same crystal structures are revealed, along the [$\bar{1}$11] directions of CoFe nanowire and nanosheet, which is located in the plane jointly determined by [110] and [101], and perpendicular to [110]. They exhibit continuous crystal structures and almost completely flat planes. In the crystallographic nature of cubic CoFe, the [110] and [1$\bar{1}$2] directions are perpendicular to each other. Taking the HRTEM and SAED (Figure 4e, 4h) images into account, the schematic illustrations of the nanowire and nanosheet with three sets of mutually perpendicular crystal planes, can be approximately derived, as shown in Figure 4i and 4j. In other words, the CoFe has two {$\bar{1}$11} flat planes, two {110} side planes and two {1$\bar{1}$2} end planes. From Figure 4f, the calculated percentage of the total surface area contributed by the set {110} planes (including (110) and its equivalent plane (1$\bar{1}$0) in the CoFe nanowire, can reach as high as 49.85%. The {$\bar{1}$11} planes are also estimated to contribute 49.85% of the total surface area. As shown in Figure 4j, the dominant exposed planes of

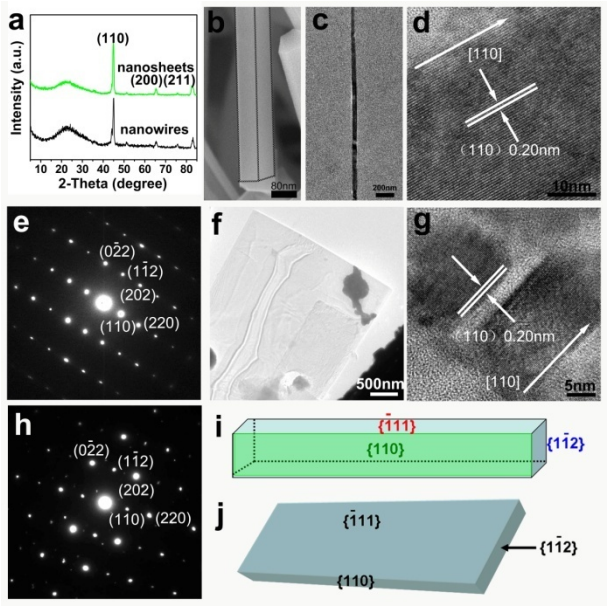

Figure 4 (a) XRD patterns of the nanowires and nanosheets after reductions; SEM (b), HRTEM(c, d) and SAED (e) patterns of the CoFe nanowire; HRTEM(f, g) and SAED (h) patterns of the CoFe nanosheet; schematic illustrations of the CoFe nanowire (i) and nanosheet (j).

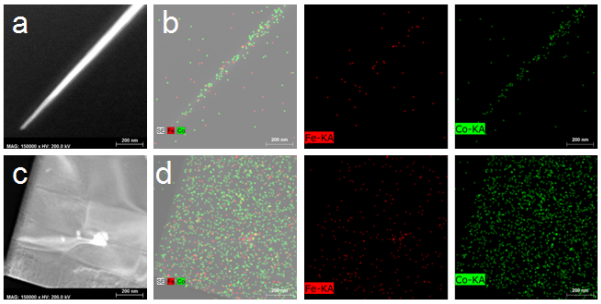

Figure 5 (a, c) STEM images of CoFe nanowire and nanosheet; (b, d) EDS compositional mapping of Co and Fe.

CoFe nanosheet are {$\bar{1}$11} planes, which are estimated to contribute 98.5% of the total surface area. The width of the nanocrystal increases from nanowire to nanosheet, on the contrary, the percentage of the surface area contributed by the {110} active planes will decrease. The compositional mapping with energy- dispersive X-ray spectroscopy (EDS) was conducted in-situ with the STEM to analyze the composition of the nanowire and nanosheet (Figure 5). The nanowire and nanosheet contained Co atoms and Fe atoms, with the Co composition being higher than Fe. The homogeneous distribution of Co and Fe is also supported by EDS elemental mapping.

Figure 6 shows the H_2-TPR profiles of the nanowires and nanosheets obtained by monitoring the signals of H_2 consumption. For the nanowires, the smaller peak centered at 311 °C can be attributed to the reduction process of Co^{3+} to Co^{2+} (step I). The larger peak centered at 439 °C with a shoulder peak can be attributed to the reduction of Fe^{2+} to Fe^0 and Co^{2+} to Co^0 (step II), respectively. However, for the nanosheets, there is one peak centered at 294 °C of step I, and the larger peak splits into two peaks (407 °C and 437 °C) in the step II. It indicates that the nanowires are difficult to reduce than nanosheets.

It is widely recognized that developing well-grown nanocrystals with a predominance of exposed regular and sharp crystal planes, still remains a great challenge. Further examination of the properties of our materials, especially in the field of specific catalysis, would be of interest. Our results provide a platform for the study of specific molecular absorption, desorption and even chemical reactions.[29, 30] Through this approach, it should be

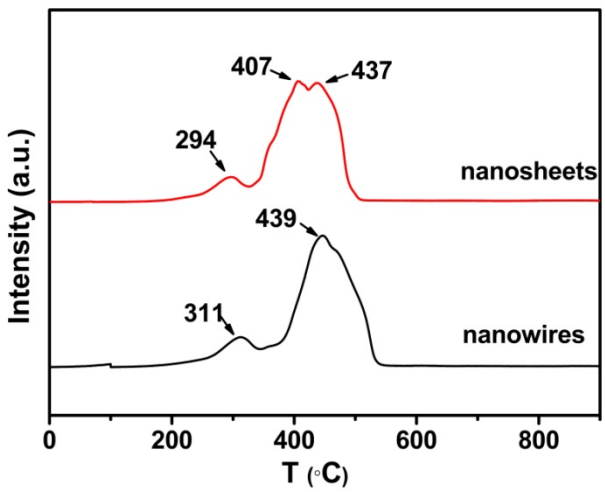

Figure 6 H_2-TPR profiles of nanowires and nanosheets.

possible to investigate the mechanisms of some significant chemical reactions at the molecular level, e.g., CO oxidation and CO hydrogenation. FT synthesis has attracted great interest due to the large variety of products that can be obtained, such as alkanes, alkenes and alcohols or narrow distributions of certain families (i. e., C_{2-4} alkenes, gasoline, and diesel).[31] Therefore, selective formation of a narrow distribution of a certain family requires a deep molecular understanding of the hydrogenation reaction and subsequent polymerization. In FT synthesis the active phase is usually made of iron or cobalt. Fe catalysts can not only be used for the production of linear alkane fuels but are also suitable for the production of alkenes or oxygenates, which are important chemical feedstocks. Fe-based catalysts exhibit much higher activity for the WGS reaction than Co-based catalysts. In addition, Fe is cheaper than Co. Compared to iron-based catalysts, cobalt-based catalysts exhibit higher stability, higher productivity.[32-34] Previous studies have shown that Fe–Co composite catalysts are efficient to produce light olefins from CO/H_2 in FT synthesis.[35] Furthermore, Fe–Co catalyst favors CoFe alloy formation and the formation of a highly dispersed CoFe alloy can increase CO conversion.[36] At last, the doping of Fe also can reduce the cost of the catalyst. Figure 7a shows the catalytic performance of multiple shaped CoFe nanocrystals for Fischer–Tropsch synthesis. A significant difference in CO conversion was observed in the CoFe nanocrystal catalysts. For a gas hourly space velocity (GHSV) of 6 $L\cdot g^{-1}\cdot h^{-1}$, the CO conversion is 44% over nanowires and 13% over nanosheets at 300 °C, with the corresponding mass specific rates of CO consumption being 10.18 and 2.98$\mu mol\cdot g^{-1}\cdot s^{-1}$, respectively. The specific rate of conversion over nanowires at 300 °C is therefore 3.42 times higher than that over nanosheets, indicting that the nanowires are significantly more active than nanosheets. At 300 °C, the turnover frequency (TOF) of Co atom on {110} planes is 8.2×10^{-2} s^{-1}, while it is only 3.2×10^{-2} s^{-1} on {$\bar{1}$11} planes. The Co sites on the {110} planes are far more reactive than those in the {$\bar{1}$11} planes. However, the BET surface area of nanowires and nanosheets is 4.7 and 25.2 $m^2\cdot g^{-1}$, respectively. Furthermore, as shown in Figure 6, the nanosheets are easy to reduce than nanowires. It indicates that the well-defined crystal plane is a significant influence factor among other factors for catalyst. The

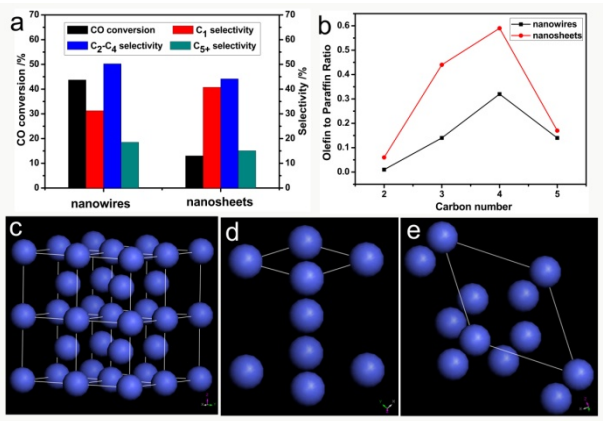

Figure 7 (a) Catalytic properties of differently shaped CoFe nanocrystals for FT synthesis; (b) carbon number effects on olefin to paraffin ratio over CoFe nanocrystals; (c) bcc structure of CoFe crystal; (d–e) the surface atomic configurations in the {110} (d) and {$\bar{1}$11} (e)planes. Reaction conditions: T=300 °C, P=2.0 MPa, H_2/CO=2, GHSV=6 $L\cdot g^{-1}\cdot h^{-1}$

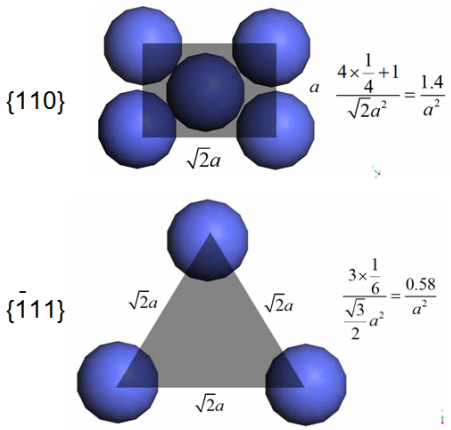

Figure 8 Surface atoms arrangement and surface atoms density of bcc CoFe Nanocrystal with different crystal planes.

CoFe nanocrystal catalysts mainly produce hydrocarbons. The selectivity of C_2-C_4 is 50% over nanowires, which is higher than that over nanosheets (44%). Methane and C_2-C_4 are the main component in the hydrocarbon products due to the high reaction temperature. Whilst the selectivity of C_{5+} over the differently shaped CoFe nanocrystals is lower. Our CoFe nanocrystals also show a higher CO conversion and light hydrocarbons selectivity for FT synthesis than previously reported cobalt- based or iron-based catalysts, as listed in Table S1. As shown in Figures 7b, the olefin/paraffin(O/P) ratio increases with increasing chain length in the C_{2-4} fraction for the nanowire and nanosheet catalysts. But the nanosheets have higher O/P ratio than nanowires. It can be found that the O/P ratio increases as the amount of Fe increase. The main reason may be the doping of Fe as a modifying additive in the CoFe nanocrystals.[37] Experimental results have indicated that with Co catalysts, FT synthesis only proceed on metallic (nonoxidized) Co species.[12, 13, 38-41] Figure 7c-7e show the representative surface atoms arrangement of the bcc CoFe nanocrystal with different crystal planes. As shown in Figure 8, the area of adjacent four brown spheres of the {110} planes is $\sqrt{2}\,a^2$, while the area of adjacent three brown spheres of the {$\bar{1}$11} planes is $\sqrt{3a^2}/2$, suggesting the {110} plane is more open than the {$\bar{1}$11} planes. Therefore, the {110} planes have a more reactive surface. The design of the CoFe nanocrystals with more reactive crystal planes being exposed is the origin of the high catalytic activity of the material. The array structure of the CoFe nanocrystals also contributes to the high activity by preventing the sintering（Figure 4g). The nanocrystal directly grown on the iron substrate can ensure efficient anchoring of the nanocrystal and prevent leaching during catalytic reactions. Furthermore, the spaces between neighboring nanocrystals are much larger, which allows for easy gas diffusion and mass transport, resulting in a high utilization of materials.

4. Conclusions

In summary, CoFe nanocrystals have been fabricated on an iron substrate by a controllable process involving the hydrothermal growth and calcinations of cobalt iron hydroxide carbonate nanowires, and subsequently the reduction of $Co_{3-x}Fe_xO_4$. Such architectures showed excellent catalytic activity for Fischer-Tropsch Synthesis, which can be related to the preferential

exposure of crystal planes with a relatively high density of active species (i.e. {110}), and the doping of Fe in situ. The properties of nanomaterials for use in catalytic, magnetic, electrocatalytic and energy storage applications have a strong dependence on their crystal orientation/ dominated exposed plane.[42-44] Nanocrystals with high-energy facets, which possess a high density of reactive surface sites and open surface structure can lead to exceptional catalytic properties. The present results suggest that specifically designed nanomaterials with predictable morphologies and exposed crystal planes by controlling synthesis parameters on metallic substrates might bring new opportunities for developing highly efficient structured catalysts.

Acknowledgements

This work was financially supported by the autonomous research project of SKLCC (Grant No. 2013BWZ004) and the NSFC (Grant No. 21373254).

Notes and references

[a] *State Key Laboratory of Coal Conversion, Institute of Coal Chemistry, Chinese Academy of Sciences, Taiyuan, 030001, China. E-mail: sunjiaqiang@sxicc.ac.cn*

[b] *State Key Laboratory of Biomass Thermal Chemistry Technology, Wuhan, 430223,China.*

† Electronic Supplementary Information (ESI) available: supplementary figures and tables. See DOI: 10.1039/b000000x/

1 M. E. Dry, *Catalysis Today*, 2002, **71**, 227-241.
2 K. Zhou, X. Wang, X. Sun, Q. Peng and Y. Li, *Journal of Catalysis*, 2005, **229**, 206-212.
3 N. Tian, Z. Y. Zhou, S. G. Sun, Y. Ding and Z. L. Wang, *Science*, 2007, **316**, 732-735.
4 R. Si and M. Flytzani-Stephanopoulos, *Angewandte Chemie International Edition*, 2008, **47**, 2884-2887.
5 J. Sun, Y. Li, X. Liu, Q. Yang, J. Liu, X. Sun, D. G. Evans and X. Duan, *Chemical Communications*, 2012, **48**, 3379-3381.
6 L. Hu, Q. Peng and Y. Li, *Journal of the American Chemical Society*, 2008, **130**, 16136-16137.
7 X. Xie, Y. Li, Z. Q. Liu, M. Haruta and W. Shen, *Nature*, 2009, **458**, 746-749.
8 X. Liu, J. Liu, Z. Chang, X. Sun and Y. Li, *Catalysis Communications*, 2011, **12**, 530-534.
9 H. Oosterbeek, *Physical Chemistry Chemical Physics*, 2007, **9**, 3570-3576.
10 Geerlings, M. Zonnevylle and C. De Groot, *Catalysis letters*, 1990, **5**, 309-314.
11 J.J.C. Geerlings, M.C. Zonnevylle, C.P.M. de Groot, *Surface Science*, 1991, **241**, 302-314.
12 J.J.C. Geerlings, M.C. Zonnevylle, C.P.M. de Groot, *Surface Science*, 1991, **241**, 315-324.
13 E. Iglesia, S. L. Soled and R. A. Fiato, *Journal of Catalysis*, 1992, **137**, 212-224.
14 J. X. Liu, H. Y. Su, D. P. Sun, B. Y. Zhang and W. X. Li, *Journal of the American Chemical Society*, 2013, **135**, 16284-16287.
15 G. Ertl, *The Chemical Record*, 2001, **1**, 33-45.
16 F. S. Bates and G. H. Fredrickson, *Physics today*, 1999, **52**, 32-38.
17 G. Ertl, *Angewandte Chemie International Edition*, 2008, **47**, 3524-3535.
18 R. Guettel, J. Knochen, U. Kunz, M. Kassing and T. Turek, *Industrial & Engineering Chemistry Research*, 2008, **47**, 6589-6597.
19 K. Pangarkar, T. J. Schildhauer, J. R. van Ommen, J. Nijenhuis, J. A. Moulijn and F. Kapteijn, *Catalysis Today*, 2009, **147**, S2-S9.
20 P. Sonstrom, M. Adam, X. Wang, M. Wilhelm, G. Grathwohl and M. Baumer, *The Journal of Physical Chemistry C*, 2010, **114**, 14224-14232.
21 F. K. Theo Vergunst, Jacob A. Moulijn, *Applied Catalysis A: General*, 2001, **213**, 179-187.
22 Wahlberg, L. J. P. , Karin Bruce, M. A. and K. J. , *Applied Catalysis B: Environmental* 1999, **23**, 271-281.
23 M. Crudden, M. Sateesh and R. Lewis, *Journal of the American Chemical Society*, 2005, **127**, 10045-10050.
24 T. Bell, *Science*, 2003, **299**, 1688-1691.
25 Q. Yang, Z. Lu, J. Liu, X. Lei, Z. Chang, L. Luo and X. Sun, *Progress in Natural Science: Materials International*, 2013, **23**, 351-366.
26 X. Huang, Z. Zhan, X. Wang, Z. Zhang, G. Xing, D. Guo, D. Leusink, L. Zheng and T. Wu, *Applied Physics Letters*, 2010, **97**, 203112.
27 Y. Xiong, Y. Xie, Z. Li, R. Zhang, J. Yang and C. Wu, *New Journal of Chemistry*, 2003, **27**, 588-590.
28 Y. Li, Q. Liu and W. Shen, *Dalton Transactions*, 2011, **40**, 5811-5826.
29 Y. Wang, Y. Ye and K. Wu, *Journal of Physical Chemistry B*, 2006, **110**, 17960-17965.
30 Y. Ye, W. Sun, Y. Wang, X. Shao, X. Xu, F. Cheng, J. Li and K. Wu, *Journal of Physical Chemistry C*, 2007, **111**, 10138-10141.
31 G.P. Van der Laan, A.A.C.M. Beenackers, *Catalysis Reviews-science and engineering,* 1999, **41**, 255-318
32 Q. Zhang, J. Kang and Y. Wang, *ChemCatChem*, 2010, **2**, 1030-1058.
33 Z. Wang, Z. Yan, C. Liu and D. W. Goodman, *ChemCatChem*, 2011, **3**, 551-559.
34 V. R. Calderone, N. R. Shiju, D. Curulla-Ferré, S. Chambrey, A. Khodakov, A. Rose, J. Thiessen, A. Jess and G. Rothenberg, *Angewandte Chemie International Edition*, 2013, **52**, 4397-4401.
35 C. Cabet, A. C. Roger, A. Kiennemann, S. Läkamp and G. Pourroy, *Journal of Catalysis*, 1998, **173**, 64-73.
36 V. A. de la Peña O'Shea, M. C. Álvarez-Galván, J. M. Campos-Martín and J. L. G. Fierro, *Applied Catalysis A: General*, 2007, **326**, 65-73.
37 A. Mirzaei, R. Habibpour and E. Kashi, *Applied Catalysis A: General*, 2005, **296**, 222-231.
38 Y. Khodakov, W. Chu and P. Fongarland, *Chemical Reviews*, 2007, **107**, 1692-1744.
39 S. Soled, E. Iglesia, R. Fiato, J. Baumgartner, H. Vroman and S. Miseo, *Topics in Catalysis*, 2003, **26**, 101-109.
40 E. Iglesia, S. C. Reyes, R. J. Madon and S. L. Soled, *Advances in Catalysis*, 1993, **39**, 221.
41 E. Iglesia, *Applied Catalysis A: General*, 1997, **161**, 59-78.
42 K. Zhou and Y. Li, *Angewandte Chemie International Edition*, 2012, **51**, 602-613.
43 X. Huang, L. Li, X. Luo, X. Zhu and G. Li, *Journal of Physical Chemistry C,* 2008, **112**, 1468-1472.
44 Z. Zhou, N. Tian, J. Li, I. Broadwell and S. Sun, *Chemical Society Reviews,* 2011, **40**, 4167-4185.